Crossover between Ballistic and Diffusive Quantum Transport in Bi_2Se_3 Nanoribbon Devices

Kiryl Niherysh [1], Nermin Trnjanin [1], Ananthu P. Surendran [1], Gunta Kunakova [1,2], Xavier Palermo [1], Domenico Montemurro [1,3], Jana Andzane [2], Donats Erts [2], Dmitry S. Golubev [4], Samuel Lara-Avila [1], Floriana Lombardi [1], and Thilo Bauch [1,*]

[1]Quantum Device Physics Laboratory, Department of Microtechnology and Nanoscience, Chalmers University of Technology, Göteborg, SE-41296, Sweden
[2]Institute of Chemical Physics, Faculty of Science and Technology, University of Latvia, Riga, LV-1586, Latvia
[3]Dipartimento di Fisica "Ettore Pancini", Università degli Studi di Napoli Federico II, Napoli, I-80125, Italy
[4]QTF Centre of Excellence, Department of Applied Physics, Aalto University, Aalto, FI-00076, Finland
[*]thilo.bauch@chalmers.se

SUPPLEMENTARY INFORMATION 1

Fabry-Pérot resonances (device C2)

Here, we examine Fabry-Pérot (FP) resonances observed in device **C2**, fabricated on the same Bi_2Se_3 nanoribbon as device **C1**, discussed in the main text. Both devices share similar dimensions: a width of $W \simeq 430$ nm and thickness $t \simeq 16$ nm, however, device **C2** has a longer junction length of $L = 100$ nm. We apply the same analysis approach as described in the main text and present the corresponding results in Fig. S1. The background-subtracted differential conductance (G_{bgr}) of the TI junction in the normal state reveals the characteristic diamond-shaped pattern associated with FP oscillations, as shown in Figs. S1(b,c). Furthermore, in the 2D-FFT provided in Fig. S1(d) exhibits two prominent peaks at frequencies of $\simeq \pm 216$ V^{-1} (corresponding to $\Delta\mu^W = 2.40$ meV) along the f_{V_b} direction. These features arise from conductance oscillations with a negative slope (highlighted by white lines) that form the diamond-shaped FP interference pattern shown in Fig. S1(c). In contrast, the peaks associated with positively sloped FP resonance lines are less pronounced than their negative-slope counterparts.

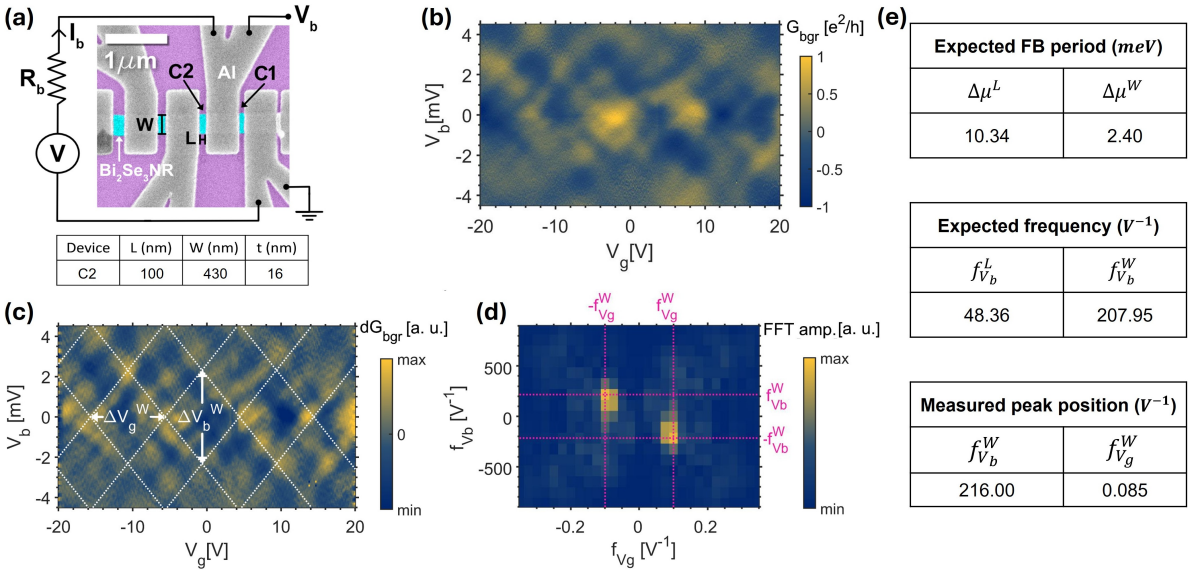

Figure S1. (a) False-colored SEM image of devices **C1** and **C2** together with the measurement layout. The dimensions of device **C2** are given in the table below. (b) Background-subtracted differential conductance map of device **C2** as a function of bias voltage V_b and back-gate voltage V_g. (c) Color map of the derivative dG_{bgr}/dV_g obtained from the conductance map from panel (b). The dashed lines indicate the expected positions of FP resonance originating from quantization along the width. (d) 2D-FFT of the color map in panel (c), showing two pronounced peaks (orange), that coincide with the expected frequencies associated with transverse quantization around the nanoribbon perimeter (magenta dashed lines). (e) Table summarizing the expected frequencies and the experimentally observed peak positions corresponding to the transverse FP resonances.

SUPPLEMENTARY INFORMATION 2

Raw conductance maps

The raw differential conductance maps in the normal state, without background subtraction, are shown in Fig. S2(a,b) for devices **C1** and **C2**, respectively. Panel (c) displays the corresponding raw data for device **C3**, measured in the superconducting state. In this case, the conductance is dominated by the critical current and sub-gap features, making it difficult to resolve additional oscillatory structures directly in the raw data. By contrast, for devices **C1** and **C2**, the oscillatory patterns observed in the raw maps are consistent with those revealed more clearly in the background-subtracted data shown in Fig.2(b) and S1(b). This agreement demonstrates that the observed Fabry-Pérot-type features are intrinsic to the devices rather than artifacts introduced by the data-processing procedure.

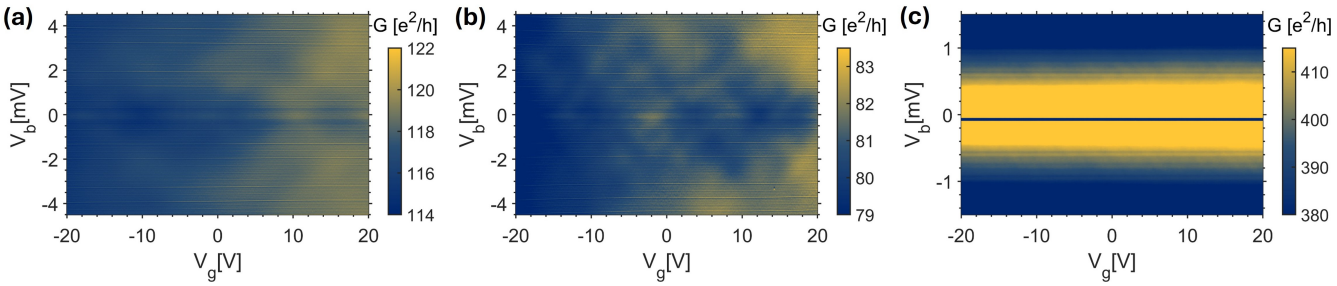

Figure S2. (a,b) Raw differential conductance maps in the normal state for devices **C1** and **C2**, respectively; and (c) the corresponding raw differential conductance map in the superconducting state for device **C3**.

SUPPLEMENTARY INFORMATION 3

Fabry-Pérot oscillations in the normal and superconducting states

To rule out the possibility that the observed magnetoconductance patterns arises primarily from UCF, we measured devices **C1** and **C2** in both the normal and superconducting states. Fig. S3 shows color maps of the derivative dG_{bgr}/dV_g as a function of bias and gate voltages, measured over a reduced gate-voltage range of $\pm$ 10 V. This range is smaller than the $\pm$ 20 V range presented in the main text and allows finer details of the oscillation patterns to be resolved. In the superconducting state (Figs. S3(c,d)), additional features appear due to the superconducting gap. Nevertheless, the FP interference pattern is preserved and remains essentially unchanged compared to the normal state (Fig. S3(a,b)). This observation demonstrates that the oscillatory features are not dominated by UCF, which would be strongly modified by the applied magnetic field.

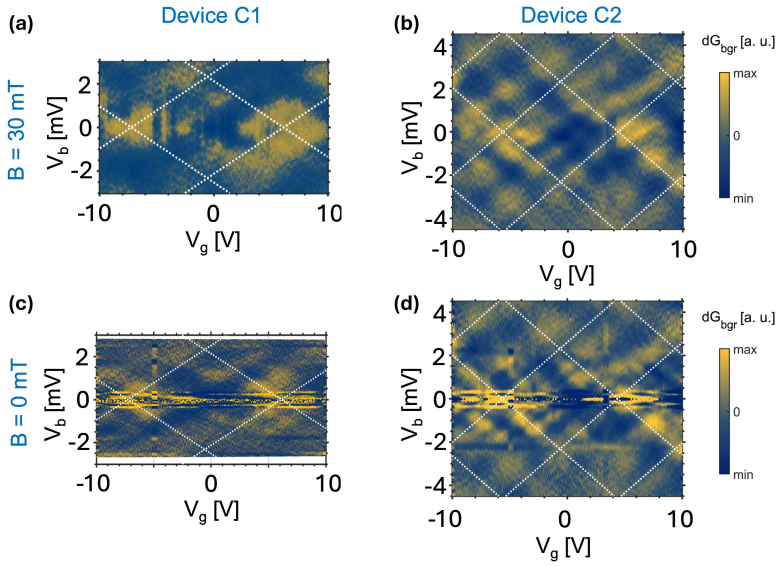

Figure S3. Color maps of the derivative dG_{bgr}/dV_g as a function of bias and gate voltages for device **C1** and **C2**, measured in the normal state ($B_{ext} = 30$ mT) and in the superconducting state ($B_{ext} = 0$ mT).

SUPPLEMENTARY INFORMATION 4

I_cR_n product and characteristic length scales

Mean free path: For the topological surface states (TSS), the electronic mean free path is given by $l_e^{TSS} = \mu\hbar\sqrt{4\pi n_{2D}}/e$, where μ is the carrier mobility, $\hbar$ is the reduced Planck constant, n_{2D} is the 2D carrier density, and e is the elementary charge. For bulk states, the mean free path is $l_e^{bulk} = \mu m^* v_F/e$, where $m^* \sim 0.15 m_e$ is the effective mass, m_e is the free-electron mass, and $v_F \sim 5 \cdot 10^5$ m/s is the Fermi velocity for a chemical potential close to the edge of the conduction band[1,2].

I_cR_n product: For a long diffusive Josephson junction $L > \xi^{diff}$ in the zero-temperature limit, the I_cR_n product is proportional to the Thouless energy $\hbar D/L^2$, where D is the diffusion constant[3]. The superconducting coherence length in the diffusive limit is given by $\xi^{diff} = \sqrt{\hbar D/\Delta'}$ with the induced superconducting gap $\Delta' \sim 160\ \mu$eV[4]. The diffusion constant is $D = v_F l_e/2$ for a 2D system and $D = v_F l_e/3$ for a 3D system. For a short ballistic Josephson junction, $L < \xi^b$, the I_cR_n product is constant and proportional to the induced gap Δ'. Here, $\xi^b = \hbar v_F/\Delta' \simeq 2\ \mu$m is the superconducting coherence length in the ballistic limit.

References

1. Kunakova, G. *et al.* Bulk-free Topological Insulator Bi_2Se_3 Nanoribbons with Magnetotransport Signatures of Dirac Surface States. *Nanoscale* **10**, 19595–19602, DOI: https://doi.org/10.1039/c8nr05500a (2018).

2. Kunakova, G. *et al.* High-Mobility Ambipolar Magnetotransport in Topological Insulator Bi_2Se_3 Nanoribbons. *Phys. Rev. Appl.* **16**, 024038, DOI: https://doi.org/10.1103/PhysRevApplied.16.024038 (2021).

3. Zaikin, A. & Zharkov, G. Effect of External Fields and Impurities on the Josephson Current in SNINS Junctions. *Zh. Eksp. Teor. Fiz.* **81**, 1781–1802 (1981).

4. Kunakova, G. *et al.* High-transparency Bi_2Se_3 Topological Insulator Nanoribbon Josephson Junctions with Low Resistive Noise Properties. *Appl. Phys. Lett.* **115**, 172601, DOI: https://doi.org/10.1063/1.5123554 (2019).